Breaking the Degeneracy: Optimal Use of Three-point Weak Lensing Statistics

Sanaz Vafaei[1], Tingting Lu[2], Ludovic van Waerbeke[1], Elisabetta Semboloni[3], Catherine Heymans[4,], Ue-Li Pen[5]

[1] *Department of Physics and Astronomy, University of British Columbia, 6224 Agricultural Road, Vancouver, BC V6T 1Z1, Canada*

[2] *Department of Astronomy and Astrophysics, University of Toronto, Canada M5S 3H4*

[3] *Argelander-Institut für Astronomie, Auf dem Hügel 71, Bonn D-53121, Germany*

[4] *Scottish Universities Physics Alliance (SUPA), Institute for Astronomy, University of Edinburgh, Royal Observatory, Blackford Hill, Edinburgh EH9 3HJ*

[5] *Canadian Institute for Theoretical Astrophysics, University of Toronto, 60 St George Street, Toronto, Canada ON M5S 3H8*

Abstract

We study the optimal use of three-point statistics in the analysis of weak lensing by large-scale structure. The three-point statistics statistics have long been advocated as a powerful tool to break measured degeneracies between cosmological parameters. Using ray-tracing simulations, incorporating important survey features such as a realistic depth-dependent redshift distribution, we find that a joint two- and three-point correlation function analysis is a much stronger probe of cosmology than the skewness statistic. We compare different observing strategies, showing that for a limited survey time there is an optimal depth for the measurement of three-point statistics, which balances statistical noise and cosmic variance against signal amplitude. We find that the chosen CFHTLS observing strategy was optimal and forecast that a joint two- and three-point analysis of the completed CFHTLS-Wide will constrain the amplitude of the matter power spectrum σ_8 to 10% and the matter density parameter Ω_m to 17%, a factor of 2.5 improvement on the two-point analysis alone. Our error analysis includes all non-Gaussian terms, finding that the coupling between cosmic variance and shot noise is a non-negligible contribution which should be included in any future analytical error calculations.

Key words: Weak Gravitational Lensing, Cosmology

1. Introduction

Weak gravitational lensing by large scale structure is a unique tool to probe the matter distribution of the Universe regardless of its dynamical state. When combined with redshift information weak lensing can be used as a probe for dark energy evolution as the expansion of the Universe affects the mass clustering at different redshifts. Dark energy constraints from weak lensing rely on accurate measurements of dark matter power spectrum amplitude. The two-point cosmic shear statistics offer a powerful technique to measure the matter normalization parameter σ_8 and the mass density parameter Ω_m combined (see for example the recent work on the CFHTLS by [1] and [2]). One of the important goals for better determination of the cosmological parameters is to improve the individual measurement of σ_8 and Ω_m. Better estimation of σ_8 and Ω_m allows for the alleviation of the residual parameter degeneracies [3]. A noticeable example is the neutrino mass [4].

Three-point shear statistics, in particular the skewness, are in principle powerful estimators to break the degeneracy between σ_8 and Ω_m ([5] and [6]). Some detections have been reported from the VIRMOS survey ([7] and [8]) and from the CTIO survey [9]. Unfortunately, the signal-to-noise ratio remains low and there are still no reliable forecasts of three-point statistics which take into the account realistic galaxy number counts and shape noise as well as non-Gaussian contributions in the cosmic variance. Therefore, the interpretation of the measurement is currently not well-established. In [10] the authors concluded that the three-point statistics of lensing signal is greatly enhanced at small angular scales because of the non-linear gravitational clustering, but they did not provide an estimate of the signal-to-noise ratio for different survey depths. In [6] it was shown that the skewness of the convergence can be measured from mass maps reconstructed from the shear measured on individual galaxies, however, a realistic population of source galaxies was not considered, and the simulations were limited to second order perturbation theory. [11] showed that one can learn additional information by combining the two- and three-point statistics, but again neither a realistic source galaxy distribution nor different survey strategies were considered. [12] also showed that combining the power spectrum and bispectrum tomography information enhances the accuracy of cosmological parameter estimations.

In this paper we investigate the optimal use of three-point statistics in a weak lensing analysis of large scale structure, considering several new aspects that have been neglected in previous works:

- A realistic noise contribution using ray-tracing simulations calibrated on existing surveys is included.

- Realistic forecasting for the two- and three-point statistics for different survey strategies is provided.

- For a fixed observing time, wide-shallow and narrow-deep strategies are considered. The impact of the survey's depth on both the galaxy number density and the source redshift distribution is quantified. Surveys

with different characteristics are affected differently by cosmic variance, with wider surveys probing a much larger number of modes than narrow surveys. Here we carefully investigate this aspect by comparing the performance of various simulated surveys which use a realistic source distribution.

- The source distribution has been derived using galaxy counting as a function of redshift as measured in real data for a fixed limiting magnitude.

- The full likelihood analysis with covariance matrices are computed from a large set of ray-tracing simulations. It is therefore an extension of previous works which used fisher matrices to gauge the performance of weak lensing surveys (e.g. [13]).

- Following [14] a comparison of different smoothing filters is included.

- A range of most optimal smoothing scales are found by investigating the various contributions of noise and signal to the full covariance matrix.

- The best survey strategy for detecting the skewness of the convergence S_3 as means of breaking the degeneracy between Ω_m and σ_8 is studied. The idea first emerged in [5] and [6] but its feasibility never quantified.

- The efficiency of combining the two- and three-point statistics is quantified.

- Two- and three-point statistics forecasts for the completed CFHTLS survey and the KIDS survey are calculated.

The paper is organised as follows. In §2, we summarize the background theory of the two- and three-point statistics of the convergence field, where notations and definitions are also introduced. The details of the method are described in §3. Optimal survey strategies are shown in §4, and §5 shows the predictions of two- and three-point measurements of the simulated complete CFHTLS-Wide survey area and depth. The upcoming KIlo Degree Survey geometry is also discussed here as an example of the accuracy achievable on the measurement of the two- and three-point statistics in the near future. Finally in §6 the conclusions of this study are stated.

2. Theory Background

Following [15] and [16] we can write the convergence κ at a given sky position θ as :

$$\kappa(\boldsymbol{\theta}) \quad = \quad \frac{3}{2} \frac{H_0^2}{c^2} \Omega_m \int_0^\infty \omega(z) \delta(\chi, \boldsymbol{\theta}) d\chi \tag{1}$$

3

where χ is the angular comoving distance, Ω_m is the mass density parameter at the present day, δ is the matter density contrast and $\omega(z)$ for a given redshift z is given by:

$$\omega(z) \quad = \quad (1+z)\chi(z) \int_z^\infty n(z_s) \left[1 - \frac{\chi(z)}{\chi(z_s)} \right] dz_s \tag{2}$$

$\omega(z)$ depends on the cosmological parameters and the galaxy source distribution function $n(z_s)$. The convergence maps are obtained from ray-tracing simulations, as described in Section 3.1.

Note that this analysis employs the convergence field κ, which is proportional to the projected mass density. The convergence can be obtained from the shear data $\gamma = (\gamma_1, \gamma_2)$ either by appropriate weighting with an aperture filter, or from mass reconstruction with e.g. a top-hat or Gaussian filter. Therefore, the conclusions of this study apply to the convergence and the shear without distinction. We are interested in the measurement of $\langle \kappa^2 \rangle$, $\langle \kappa^3 \rangle$ and the skewness $S_3(\kappa)$ defined as:

$$S_3 = \frac{\langle \kappa^3 \rangle}{\langle \kappa^2 \rangle^2}. \tag{3}$$

Skewness is essentially a measure of the clustering of the mass distribution as defined in [5]. According to perturbation theory S_3 provides a measurement of Ω_m independent of the normalization of power spectrum σ_8. For this reason, the skewness of the convergence appears as a very attractive probe of cosmology and a useful technique to break degeneracies among other cosmological parameters.

3. Analysis Method

3.1. Ray-tracing Simulations

This analysis is based on a set of simulated κ-maps, with 60 lines of sight each containing 40 redshift slices from $z = 0.020$ to $z = 3.131$. These are generated from 22 independent N-body simulations by randomization. As a result, the different lines of sight are not totally independent on large scales. However they can still be considered approximately independent on scales smaller than 1 degree.

The Multiple Lens-Plane ray-tracing approximation method was used to generate the lensing convergence map: the dark matter distribution in the universe is approximated by a series of mass sheets. The N-body simulations are on a grid of 1728^3 points with 856^3 particles, and the box size is $120 \ h^{-1}$Mpc. The mass density in the simulation box is projected to the mid-plane at a series of characteristic redshifts. The output redshifts are picked so that the consecutive time slices can represent the continuous evolution of the large scale structure. The three orthogonal axes of the box are x, y, and z. For every output redshift, we make three projection sheets, parallel to the xy, yz and xz planes. We choose one projection sheet out of the three of one N-body simulation in a
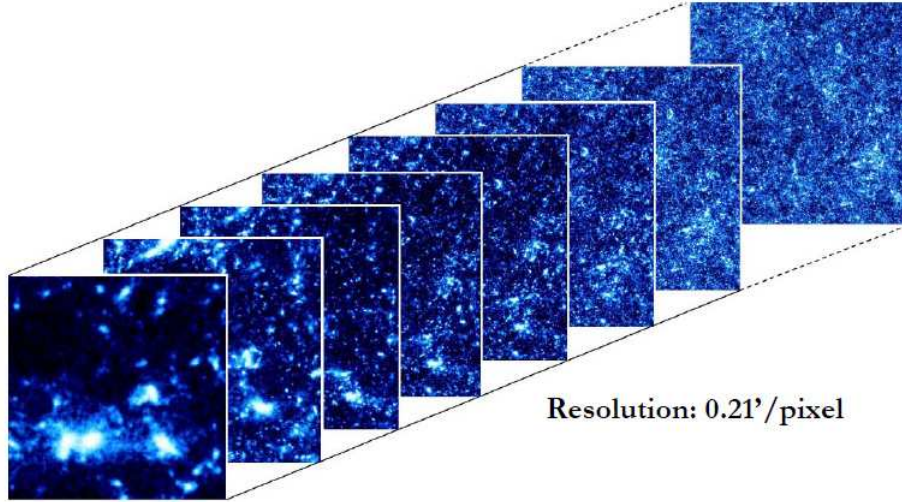
Figure 1: A schematic of the simulated convergence maps at different redshift slices. The maps are on 1024^2 with 0.21 arcmin per pixel. The redshift ranges from z=0.020 to z=131.

random order, as well as randomly shifting the sheet transverse to the projection direction. This technique is employed to avoid creating periodicity in the projection. Rays are shot through these mass sheets. We calculate κ on every sheet and project them along lines of sight after the random shift and rotation.

The maps are on $1024{\times}1024$ grid with spacing of 0.21 arcmin. Thus the total area is about 12.84 deg^2 for each line of sight. We assume the following cosmology: Λ_{CDM} with $\Omega_m = 0.24$, $\Omega_\Lambda = 0.76$ and $\sigma_8 = 0.74$ [17]. Figure 1 shows a schematic of the different redshift slices which were combined for each line of sight.

The N-body simulations are generated by the CUBEPM code, which is the successor of PMFAST [18]. CUBEPM is MPI parallelized particle-mesh (PM) code, and has particle-particle force implement at sub-grid scales. It is further parallelized by shared-memory OpenMP on each node. The simulation volume (which is also called simulation box) is cubically decomposed to n^3 sub-volumes, and the calculation of each sub-volume is performed on one node of the cluster. The total number of nodes used in simulation is n^3 with $n = 3$ here. The code can be run on up to 1000 nodes. The simulations are run on the Sunnyvale cluster of CITA.

For each of the redshift slices the average $\langle\kappa^2\rangle$, $\langle\kappa^3\rangle$ and S_3 are measured and the signal is compared with a theoretical model. The two-point cosmological predictions are based on the Peacock and Dodds [19] non-linear fit, whereas the three-point shear statistics predictions use the bispectrum non-linear fit derived in [20] and implemented for lensing studies in [10]. The excellent agreement between the measured and the predicted signal can be seen in figure 2 where
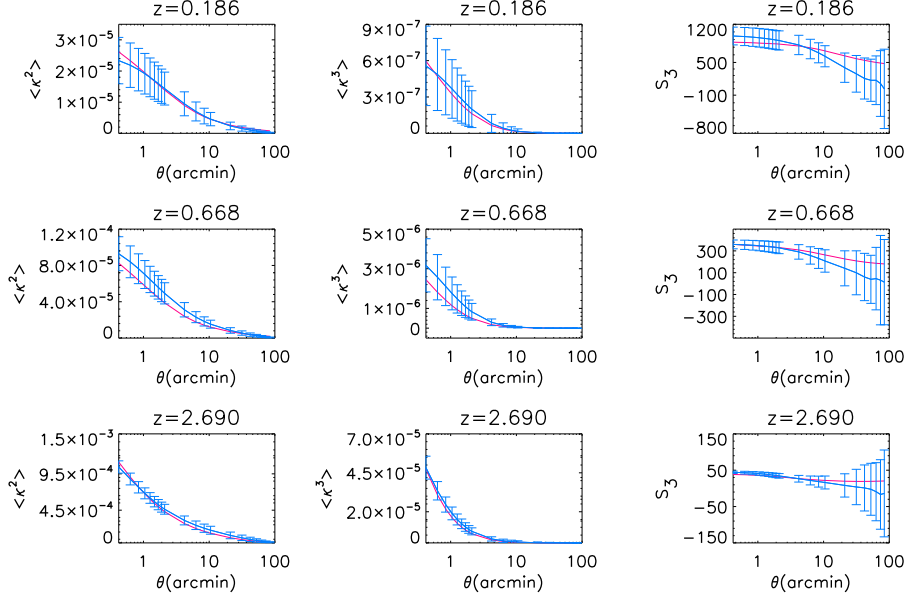
5

Figure 2: The agreement between the measurements and the theoretical predictions for three individual redshift slices. The low redshift slice is at 0.186, the medium slice at 0.668 and the high redshift slice is at z=2.690. The blue lines show the measurements on the simulated 12.84 deg^2 data, and the pink lines show the theoretical prediction for the same cosmological model at the same redshift. The measurements in each panel are made from data smoothed with a top-hat filter. The errorbars represent the cosmic variance over 60 lines of sight.

the results for low, intermediate and high redshift slices are shown.

3.2. Galaxy Number Density and Redshift Distribution

In this paper we compare different survey strategies with varying source redshift distribution that is dependent on the survey depth. We calibrate the redshift distribution from existing optical surveys with photometric redshift information and populate the ray-tracing slices accordingly. The focus here is on ground based surveys, but the result can be straightforwardly extended to space data with an appropriate scaling of the shot noise (which directly depends on the galaxy shape noise and number density).

The galaxy number density and redshift distribution as a function of limiting magnitude are estimated from the CFHTLS-Deep survey catalogue in i-band [21]. To model the galaxy redshift distribution $n(z)$ for surveys of different magnitude limit $\mathrm{m_{lim}}$, the method described in [22] and [23] was employed, modeling $n(z, \mathrm{m_{lim}})$ as:

$$n(z, \mathrm{m_{lim}}) = \frac{\beta}{z_0 \Gamma\left(\frac{1+\alpha}{\beta}\right)} \left(\frac{z}{z_0(\mathrm{m_{lim}})}\right)^{\alpha} \exp\left[-\left(\frac{z}{z_0(\mathrm{m_{lim}})}\right)^{\beta}\right] \qquad (4)$$
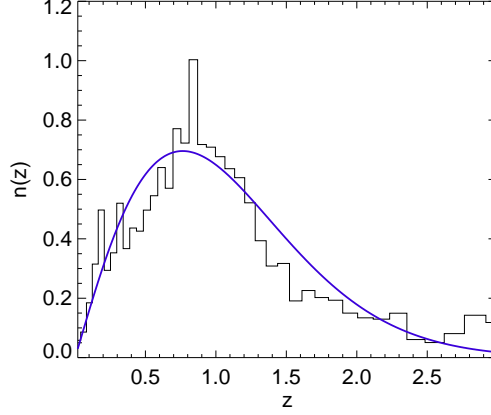
6

Figure 3: The fit to the normalized galaxy number density from the CFHTLS-Deep survey catalogue [21]. The black line shows the histogram of the galaxy number density and the dark blue line is the fitted curve. The limiting magnitude m_{lim} =24.5 with the fitting formula given by equation (4). Here α, β and z_0 are 0.96, 1.70 and 1.07 respectively.

The best parametric fit to equation (4) for limiting magnitude i =24.5 corresponds to α=0.96, β=1.70 and z_0=1.07. Figure 3 shows the histogram of the normalized galaxy redshift distribution from the CFHTLS-Deep survey catalogue [21] at m_{lim} =24.5 and the best fit $n(z)$ from equation (4). Table 1 summarizes the values of α, β, z_0 and the median redshift z_{med} for the other magnitude cuts used in this paper. Equation (4) yields a realistic source redshift distribution for a given survey's depth [23]. Thus, the theoretical predictions built based on the appropriate form of equation (4) match the κ-maps weighted by the galaxy number density derived from the CFHTLS-deep catalogues.

m_{lim}	α	β	z_0	z_{med}
22.5	0.76	6.85	1.05	0.68
23.0	0.71	5.30	1.14	0.72
23.5	0.81	3.15	1.19	0.80
24.0	0.80	2.72	1.26	0.84
24.5	0.96	1.70	1.07	0.91
25.0	0.85	1.90	1.26	0.96
25.5	1.46	1.30	0.75	1.02
26.0	1.71	1.27	0.68	1.04

Table 1: The best fit values of α, β and z_0 corresponding to equation (4) for several i-band limiting magnitudes. These parameters were used to generate theoretical models for Section 4 to determine the best survey strategy. The last column contains the median redshift z_{med} for each magnitude cut.

3.3. Statistical Noise

The source of shot noise in weak lensing studies depends on the intrinsic ellipticity characterized by the r.m.s. σ_ϵ and by the number density of galaxies n_g. It was shown in [24] that the noise in a smoothed convergence map can simply be derived from the intrinsic ellipticity noise and the galaxy number density. In particular, it was shown that the noise in a pixelated smoothed κ map is simply given by a smoothed uncorrelated Gaussian noise with r.m.s. σ_ϵ. If n_g denotes the number density of galaxies and $W(\boldsymbol{\theta})$ the 2-dimensional smoothing function, then the correlation function of the convergence noise is:

$$\langle \kappa_n(\boldsymbol{\theta})\kappa_n(\boldsymbol{\theta}')\rangle = \frac{\sigma_\epsilon^2}{2}\frac{1}{\Theta^2 n_g}\int d\mathbf{k}e^{i\mathbf{k}\cdot(\boldsymbol{\theta}-\boldsymbol{\theta}')}\left|\tilde{W}(\mathbf{k})\right|^2 \tag{5}$$

where $\kappa_n(\boldsymbol{\theta})$ is the convergence noise map and $\tilde{W}(\mathbf{k})$ is the Fourier transform of the smoothing window $W(\boldsymbol{\theta})$. Θ is the pixel size, so $\Theta^2 n_g$ is the average number of galaxies per pixel.

The galaxy ellipticity r.m.s. measured on CFHTLS-deep data is $\sigma_\epsilon^2 = (\sigma_{\epsilon_1}^2 + \sigma_{\epsilon_2}^2) = 0.44$. For the purpose of this paper we will assume that σ_ϵ is constant as a function of redshift and galaxy type. The convergence noise variance per pixel (before smoothing with W) is therefore given by:

$$\sigma_\kappa^2 = \frac{\sigma_\epsilon^2}{2}\frac{1}{\Theta^2 n_g} \tag{6}$$

Note that the noise model considered here implicitly assumes sources galaxies are distributed randomly in each redshift slice. By construction, this choice ignores any potential effect caused by source clustering, which is known to be a source of contamination for three-point statistics ([25] and [26]).

3.4. Smoothing Filters

Convergence statistics can be measured from smoothed κ-maps (which can be obtained from smoothed shear maps from the data). Various statistics can be build by using different smoothing filters. Following the widely accepted choice the top-hat, and two types of the compensated (the total area under the filter window is equal to zero) filters were considered. The two compensated filters used were the ones introduced in [27] (hereby referred to as the aperture filter) and in [28] which hereby referred to as the Compensated Gaussian (CG). They are defined as:

$$\begin{aligned}W_{\mathrm{ap}}(\theta) &= \frac{9}{\pi}\left(\frac{1}{\theta_f}\right)^2\left[1-\left(\frac{\theta}{\theta_f}\right)^2\right]\left[\frac{1}{3}-\left(\frac{\theta}{\theta_f}\right)^2\right] \text{ if } \theta < \theta_f \text{ zero otherwise}\\ W_{\mathrm{CG}}(\theta) &= \frac{1}{2\pi\theta_f^2}\left[1-\left(\frac{\theta^2}{2\theta_f^2}\right)\right]\exp\left(-\frac{\theta^2}{2\theta_f^2}\right)\end{aligned} \tag{7}$$

where θ_f is the characteristic size of the filter. Figure 4 shows the excellent agreement between the ray-tracing simulation and the predictions for different smoothing filters. The measurements are based on a realistic redshift
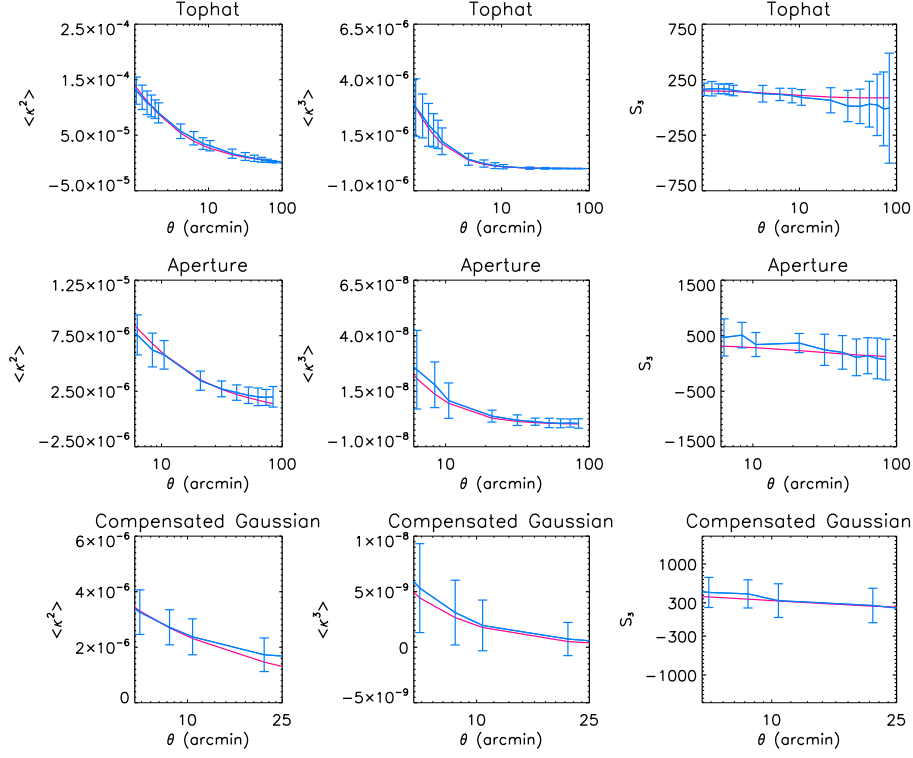
Figure 4: The agreement between the measurements and the theoretical predictions based on the fitted galaxy population. The blue lines show the measurements on the simulated 12.84 deg^2 data, and the pink lines show the theoretical prediction for the same cosmological model and the full redshift distribution. The measurements in each panel are performed on smoothed data, with top-hat, aperture mass and Compensated Gaussian filters in order. The errorbars include both cosmic variance and statistical noise resulting from $n_g = 22$ galaxies per arcmin^2.

distribution corresponding to a ground based survey with limiting magnitude $m_{\lim} = 24.5$ with $n_g = 22$ galaxies per arcmin^2. The error bars reflect the statistical noise and cosmic variance for a 12.84 deg^2 survey. From equation (7) the smoothing scale for the two filters are related as $\theta_{CG} = \theta_{ap}/2\sqrt{2}$, therefore the maximum smoothing scale chosen for the Compensated Gaussian filter is 25 arcminutes compared to 84 arcminutes for the top-hat and aperture filters.

3.5. Estimate of the Covariance Matrix

Cosmological parameter forecasting requires the estimate of the covariance matrix. Semi analytical methods are available in the literature ([31] and [32]), but rely on the assumption of Gaussian statistics. An extension to the non-linear angular scales has been recently developed ([33], [34] and [35]), however the three-point statistics and source redshift distribution and shape noise of

realistic surveys were not considered. In this work the full covariance matrix $\mathbf{C}$ was estimated directly from the ray-tracing simulation as in [33] and [34], by taking into account the realistic characteristics of lensing surveys described in the previous sections. For each survey strategy, the total covariance matrix was calculated as follows: for each noise-free κ line of sight, the redshift slices were combined and weighted according to equation (1) with the corresponding redshift distribution and galaxy number density. A noise map was then added following the method described in Section 3.3. Finally, the two- and three-point statistics were measured over 20 smoothing scales. The covariance matrix of the statistic x measured at two smoothing scales θ_i and θ_j is defined as:

$$\mathbf{C}(\theta_i, \theta_j) \equiv \langle (x(\theta_i) - \mu(\theta_i))(x(\theta_j) - \mu(\theta_j)) \rangle \tag{8}$$

where x is here either $\langle \kappa^2 \rangle$, $\langle \kappa^3 \rangle$ or S_3 and μ is the average calculated from the entire simulation set.

It was shown by [36] that the inverse of the covariance matrix estimated from a finite number of ray-tracing simulations is biased. The authors derived a simple formula to correct for this effect which relates the number of scales p used in the two- (or three-) point statistics and the number n of lines-of-sights. The covariance matrix simply has to be replaced by $\alpha^* \mathbf{C}$, where α^* when the mean is determined from the data, is given by:

$$\alpha^* = \frac{(n-1)}{(n-1) - p - 1} \tag{9}$$

[36] showed that this correction is applicable only when $n-2$ exceeds the number of scales p, otherwise the covariance matrix $\mathbf{C}$ is not invertible. In this paper $n = 60$ simulations were used, and the statistics were measured over $p = 20$ angular scales for top-hat and aperture filter and $p = 14$ for the Compensated Gaussian filter. The values of α^* for these filters were then 1.55 and 1.28 respectively. For joint likelihood calculations the joint covariance matrices were rescaled by $\alpha^* = 3.28$ for top-hat and aperture filters and $\alpha^* = 1.97$ for the Compensated Gaussian filter.

Because of the limited area covered by the simulations it is not possible to compute the covariance matrices for very large surveys. Fortunately, the angular scales where the non-linear effects are important (typically less than half a degree for the two- and three- point statistics) are much smaller than the 12.84 deg^2 field-of-view of a simulation field. Those are also the scales where the lensing signal is best measured. Therefore the covariance matrices can be computed in the non-linear regime from the different realizations, and simply rescaled according to survey size for surveys exceeding the simulation box. This is an excellent approximation for angular scales much smaller than the simulation box, which was the case in our study since the largest scale used to measure the statistics was 84 arcminutes, which is much smaller than the dimension of 3.5×3.5 degrees of the simulations box. Figure 5 illustrates the scaling applied to some elements of the two- and three-point statistic covariance matrices.
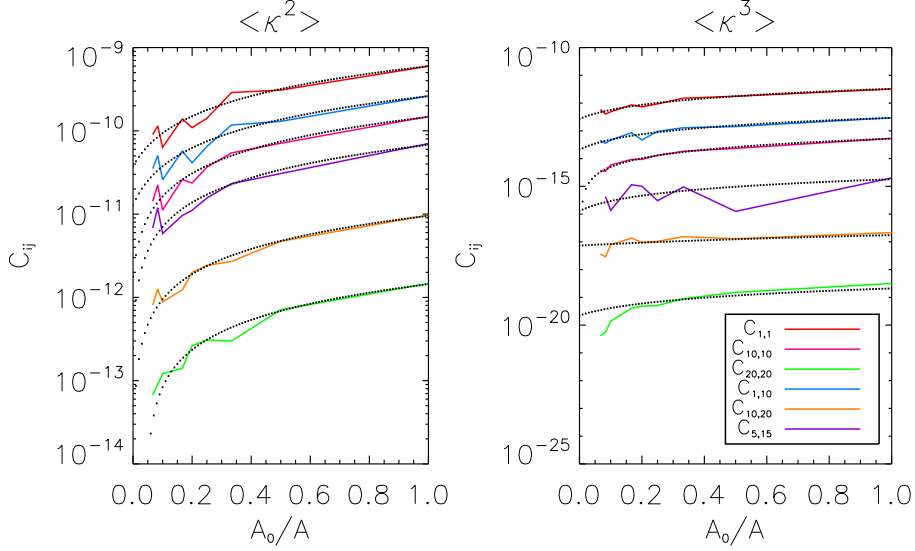
10

Figure 5: The C_{ij} elements of the covariance matrix as a function of the ratio of the original κ-map simulation area (12.84 deg^2) over the survey area. The solid colored lines are the C_{ij} elements from the simulated maps and the black dotted lines are the straight line fit to each of them. The left figure shows the C_{ij} of $\langle\kappa^2\rangle$ and the right one is the same for $\langle\kappa^3\rangle$. Here the covariance matrix contains only the cosmic variance. The scales are as following: i=1 is 0.42', i=5 is 1.26', i=10 is 4.20', i=15 is 31.5' and i=20 is 84.0'. It shows that the change in the covariance matrix of the cosmic variance is inversely proportional to the survey area. Hence this result was used to rescale the covariance matrices in the likelihood calculation to the desired survey area.

In order to verify that the covariance matrix computed using ray-tracing simulations converges to the one computed in the Gaussian approximation for large angular scales, the following procedure was performed: Gaussian realizations of the field κ were generated and then the covariance matrix was calculated in the same way as the ray-tracing simulations. [29] and [30] described a simple way to generate cosmological Gaussian fields by convolving white-noise with a filter whose transfer function is given by the square root of the power spectrum. The power spectrum was directly computed from the sample of ray-tracing simulations, so that the resulting Gaussian fields have the same cosmology. Using this method, 60 lines of sight were generated and the covariance matrix of the Gaussian fields was computed as described by equation (9). Figure 6 shows the ratio of the non-Gaussian to Gaussian errors (i.e. the square root of the diagonal elements of the covariance matrix) for the two- and three-point statistics of the top-hat and Compensated Gaussian filters. It can be seen that for large scales the ratio converges to unity as expected. At small scales this ratio is larger than the unity due to the non-linear evolution of matter fluctuations. Moreover, for a given angular scale, the ratio between non-Gaussian and Gaussian errors is larger when one uses the Compensated Gaussian filter than when the top-hat
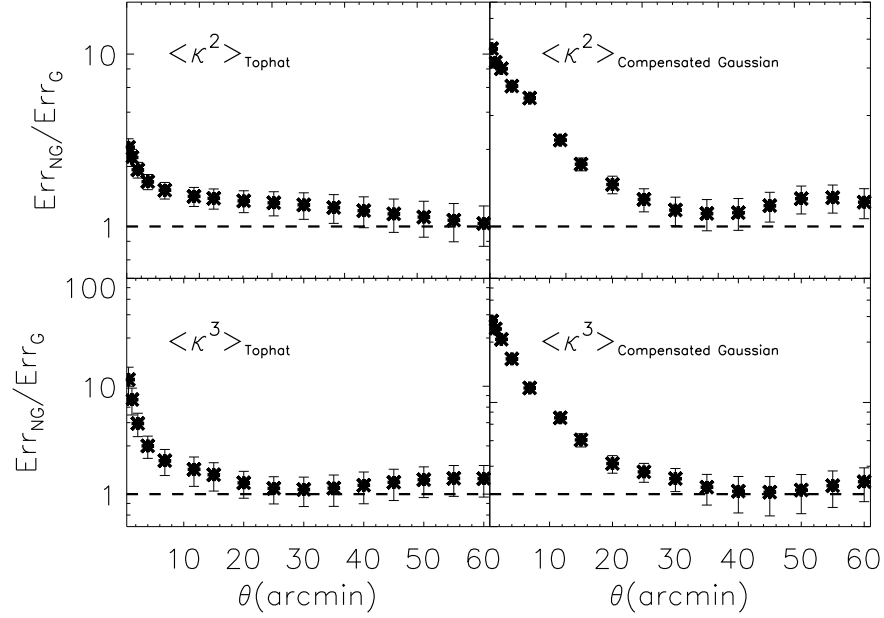
11

Figure 6: The ratio of Gaussian to non-Gaussian error estimated for convergence κ two- and three-point statistics. On large scales the non-Gaussian errors estimated from the ray-tracing simulations converge to the Gaussian limit. The results for the top-hat and Compensated Gaussian filters are shown in left and right column respectively.

filter is used. The reason lies in the fact that for a given characteristic scale, the Compensated Gaussian filter peaks at smaller scales than the top-hat filter. The ratio between non-Gaussian and Gaussian covariance depends on the average redshift of the survey and for this test a distribution characterized by an average redshift $z \sim 1.4$ was used. The ratio would have been much higher if a much shallower survey was chosen.

4. Survey Design and Observing Strategy

4.1. Optimal smoothing scale

The covariance matrix contains three terms ([31]) :

$$\mathbf{C} = \mathbf{C}_{ss} + \mathbf{C}_{ns} + \mathbf{C}_{nn} \tag{10}$$

where $\mathbf{C}_{ss}$ is the pure signal (i.e. noise free) cosmic variance, $\mathbf{C}_{nn}$ is the pure noise covariance and $\mathbf{C}_{ns}$ is the cross-correlation term. The goal in this section is to determine at which angular scale the measurement of the two- and three-point shear statistics has a better signal-to-noise ratio. For this purpose the

covariance matrix was separated into the three terms introduced above and their amplitudes for different filters were explored. Practically $\mathbf{C}_{ss}$ can be calculated from the noise free ray-tracing realizations and $\mathbf{C}_{nn}$ from noise-only convergence maps. Among the three parts of the covariance matrix: $\mathbf{C}_{ss}$, $\mathbf{C}_{nn}$, and $\mathbf{C}_{ns}$, the mixed term $\mathbf{C}_{ns}$ is the most computationally expensive to calculate. The reason is that the noise contribution to the covariance matrix converges more slowly than the cosmic variance contribution, and in practice, it is necessary to estimate the noise from more than 60 noise realizations. For the two-point statistics there are analytical formulae in [31], but there is currently no equivalent for the three-point statistic and the skewness of the convergence. In order to inspect the three different terms, the covariance matrix was calculated as follows: for each noise realization, a $\mathbf{C}$ was calculated, which was relatively noisy because it was obtained from one noise pattern. Then the average of $\mathbf{C}$ was taken over ten noise realizations. The covariance matrix thus obtained was specialized for a given noise statistical property, and the whole calculation was repeated each time the observing conditions affecting the noise were changed. $\mathbf{C}_{nn}$ was calculated separately over ten thousand realizations. The average $\mathbf{C}_{ss}$ and $\mathbf{C}_{nn}$ were used to determine the cross term $\mathbf{C}_{ns}$. Because of the averaging process one obtains a covariance matrix which has a relatively small noise making $\mathbf{C}$ invertible. To illustrate the contribution of each of these parts the diagonal elements of the $\mathbf{C}_{ss}$, $\mathbf{C}_{nn}$, $\mathbf{C}_{ns}$ and $\mathbf{C}$ were extracted as the noise term for each smoothing scale.

Figure 7 shows the relative contribution of different terms in the covariance matrix. The noise-to-signal ratio for the individual components of the covariance matrix are shown. The blue (long dashed) line is the signal-signal which is the result of the cosmic variance only. The noise-noise term is shown with black (short dashed) line. The mixed term was derived from $\mathbf{C} - \mathbf{C}_{ss} - \mathbf{C}_{nn}$ and is shown in red (dash-dotted) line and the green (solid) line shows the total noise over signal ratio. As expected the finding was that small scales were dominated by statistical noise and the large scales by cosmic variance, where the signal is low. Interestingly, the mixed noise term is relatively negligible for the two- and three-point statistics, although it is clear that future high precision surveys will have to take it into account. Surprisingly, the mixed noise term is strongly dominant for the skewness.

In agreement with [14] a range of optimal angular scales (between one arcminute and half a degree) was found for which the total noise affecting the two-point shear statistics is minimal, this is also the case for the three-point statistics.

4.2. Wide and Shallow versus Deep and Narrow

Many of the future lensing surveys will have a limited observing time and a full sky coverage will not be possible. The question will arise whether a deep and narrow survey performs better than a large and shallow survey. Therefore, it is important to quantify what is the optimal balance between survey size and depth, given a fixed observing time. It is expected that very shallow surveys
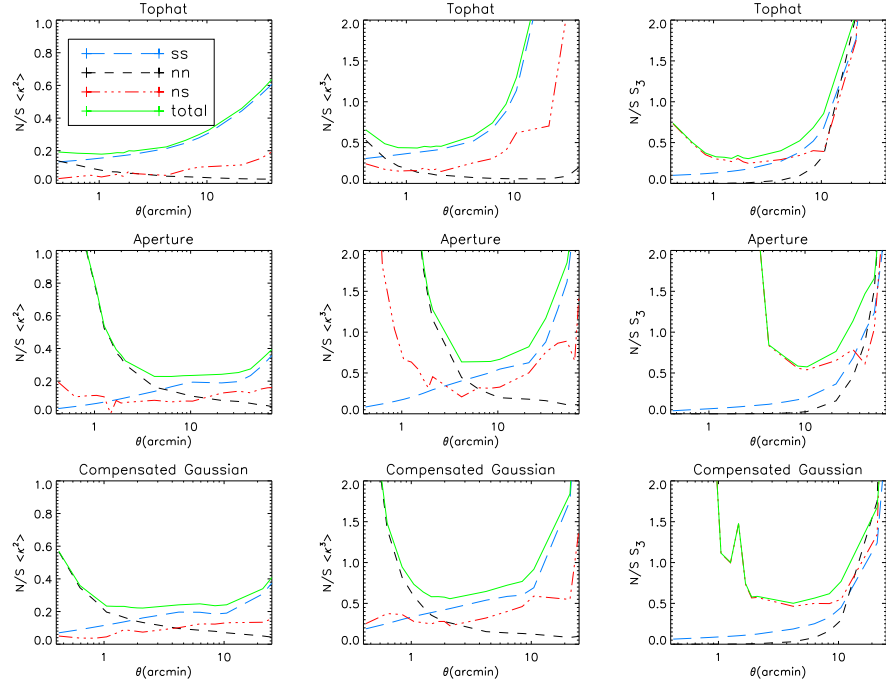
Figure 7: The noise-to-signal ratio for the cosmic variance only in blue (long dashed) line, statistical noise only in black (short dashed) line, the mixed term in red (dash-dotted) line and the total noise in green (solid). The $\langle\kappa^2\rangle$, $\langle\kappa^3\rangle$ and S_3 measurements were calculated for a simulated 12.84 $\deg^2$ data smoothed with top-hat, aperture and Compensated Gaussian (from top to bottom).

14

Area(deg^2)	1400	1150	900	514	257	115	45	20
m$_{\text{lim}}$	22.5	23.0	23.5	24.0	24.5	25.0	25.5	26.0
n$_{\text{g}}$/arcmin^2	2	5	9	14	22	28	37	45
GF	1.8	4.0	5.0	2.5	2.4	1.5	1.3	$-^\star$

Table 2: The area and i-band limiting magnitude and the corresponding galaxy number density of different surveys with the same observing time. The gain factor GF is the ratio between the Ω_m 1σ width of the two-point statistics contours over that of the two- and three-point statistics joint contour. ($\star$) Due to the truncated likelihood 1σ contours the GF is not calculated for the deepest survey.

would provide a poor weak lensing measurement due to the small lensing efficiency for nearby sources, and deep-narrow surveys will be limited by cosmic variance. The trade-off between those radically different survey designs must include a proper estimate of the amplitude of the lensing signal and shot noise as function of survey depth.

The relation between limiting magnitude and survey area for a fixed observing time was derived from the algorithm developed in [37]. The galaxy number density was obtained by selecting galaxies which signal-to-noise detection level was larger than 7 and which are also well resolved for weak lensing studies following the criteria given in Section 3.2. Table 2 shows the survey area and limiting magnitude for each case investigated here.

The likelihood is given by:

$$\mathcal{L} = \exp\left[-\frac{1}{2}(d-m)^T * \mathbf{C}^{-1} * (d-m)\right] \tag{11}$$

where d is the data and m is the theoretical model. $\mathbf{C}^{-1}$ is the inverse covariance matrix over all lines of sight. As described in the previous section the covariance matrix was computed directly by using the simulations and its inverse had been re-calibrated using equation (9). The likelihood contours were performed in the Ω_m-σ_8 parameter space. Ω_m was varied between 0.1 and 1.0 with 0.05 intervals and σ_8 values were between 0.50 and 1.50 with 0.05 intervals.

Figure 8 shows the pink (dark gray) contours for $\langle\kappa^2\rangle$ and cyan (light grey) for $\langle\kappa^3\rangle$ likelihood for top-hat filter. The filled contours show the joint $\langle\kappa^2\rangle$-$\langle\kappa^3\rangle$ likelihood. The $\langle\kappa^2\rangle$ and $\langle\kappa^3\rangle$ contours become more degenerate for deep and narrow surveys, whereas for wide and shallower surveys it appears clearly that the $\langle\kappa^2\rangle$ and $\langle\kappa^3\rangle$ likelihood contours have a different orientation in the Ω_m-σ_8 plane, which explains why the joint analysis works better for wide and shallow surveys. One can see indeed that the individual two- and three-point statistics contours for the wide and shallow surveys become large again due to a larger noise, but the joint analysis remains competitive. This could be attributed to the larger sensitivity of the three-point statistics to non-linear effects for shallow surveys as a consequence of the projection of mass along the line-of-sight (i.e. identical angular scale probes more non-linear scales for shallow rather than deep survey). For the joint two- and three-point statistics analysis, the medium depth surveys (m$_{\text{lim}}$ =23.5 or 24.0) appear optimal. It is clear that for a fixed

observing time, our results favor the medium shallow-wide surveys. The gain factor GF is defined as the ratio of the 1σ error width of the $\langle\kappa^2\rangle$ contours over that of joint $\langle\kappa^2\rangle$-$\langle\kappa^3\rangle$ measurements which quantifies the improvement when the joint statistics is considered. The values of the GF corresponding to the likelihood contours of figure 8 are shown in table 2.

Unfortunately, the skewness of the convergence, defined in equation (3), does not appear to yield as powerful constraints as the combined two- and three-point statistics. Figure 9 shows the error contours using S_3 for three choices of limiting magnitude and survey area. The observing time here was fixed, like for the previous analysis. As expected, the dependence on σ_8 is very weak, but one can see that the width of the contours along the Ω_m axis is much larger than the Ω_m constraints one gets from the joint analysis shown in Figure 8. Following the same trend as joint $\langle\kappa^2\rangle$-$\langle\kappa^3\rangle$ likelihood results shown in figure 8, the medium depth surveys lead to the most optimal skewness measurement. The constraints for the shallower surveys (i.e. m_{lim} =22.5 and 23.0) are not shown here. Those surveys give poor cosmological constraints, as the mixed $\mathbf{C_{ns}}$ term of the covariance at the scales of interest becomes large. Overall, the skewness does not appear to be as attractive a statistic to break the σ_8-Ω_m degeneracy as previously advocated ([5] and [6]). Measuring the skewness on the current and near future lensing surveys will be very challenging, and it is clear that a large fraction of the sky is needed in order to bring the noise contributions to a low enough level for precision cosmology.

The reason why the skewness is hard to measure lies in the fact that the variation of the skewness amplitude for different Ω_m models is largely absorbed by the cosmic variance of this estimator. This is not the case for the two- and three-point statistics taken separately. Figure 10 shows the comparison between various predicted cosmological models and the measurements from the simulations. $\langle\kappa^2\rangle$, $\langle\kappa^3\rangle$ and S_3 were measured for survey area of 12.84 $\deg^2$ of limiting magnitude of 24.5 over the 60 lines of sight. The blue line shows the measured data points; the errorbars contain both cosmic variance and statistical noise. The pink (solid) line is the fiducial model (Ω_m=0.24, Ω_Λ=0.76 and σ_8=0.74). The black (dotted), green (dashed) and red (dash-dotted) lines are models with the same $\sigma_8 = 0.75$ and values of $\Omega_m = 0.20, 0.40$ and 0.80 respectively, while the purple (dash-dot-dotted) line corresponds to a model with $\Omega_m = 0.30$ but $\sigma_8 = 0.50$. The plot shows that the measurement of $\langle\kappa^2\rangle$ and $\langle\kappa^3\rangle$ are much more sensitive to the Ω_m, σ_8 parameters than the skewness S_3, therefore their ability to separate various cosmological models is stronger.

5. Canada-France-Hawaii Legacy Survey Three-point Statistics Predictions

The Canada-France-Hawaii Telescope Legacy Survey covers 170 $\deg^2$ in four patches [2]. Measurements of the two-point cosmic shear statistics have been published using the first year ([38], [39] and [1]) and third year data release [2] in addition to studies of galactic scale dark matter halos [40]. In this study
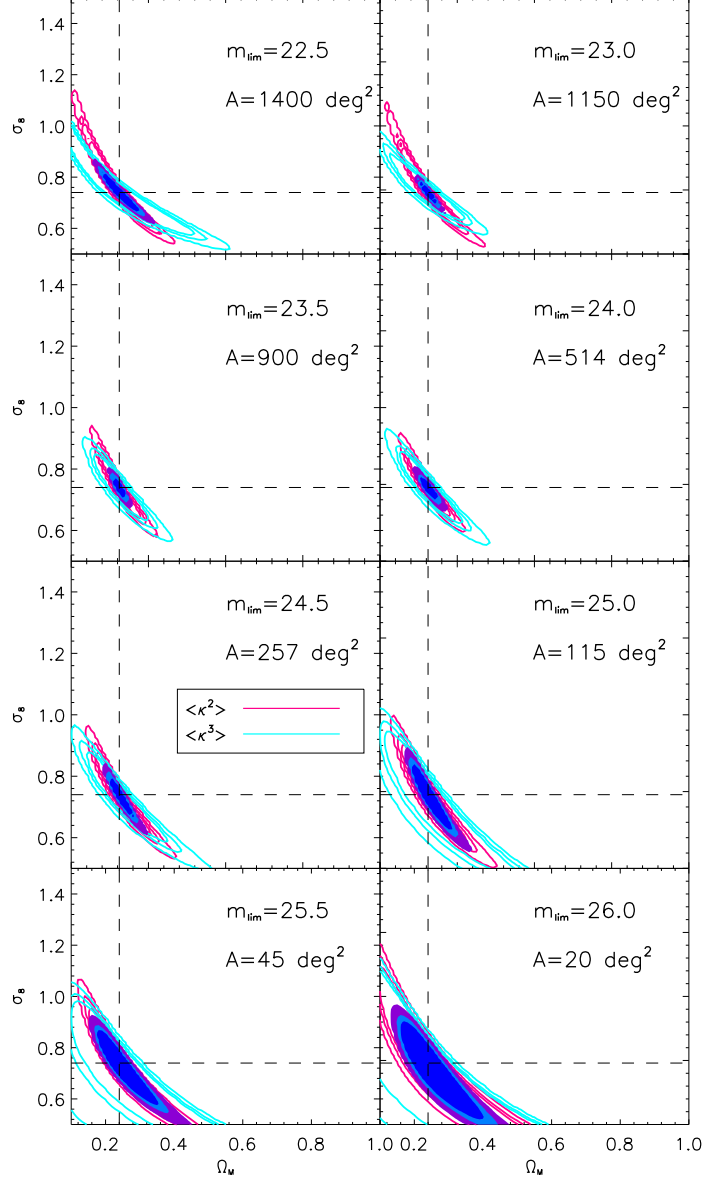
Figure 8: The likelihood analysis for various survey depths and areas with fixed observing time for $\langle\kappa^2\rangle$, $\langle\kappa^3\rangle$ smoothed with the top-hat filter. The observing time is equal for all cases, while the survey area and depth vary. Table 2 shows the values for m_{lim} with the corresponding survey areas. The pink (dark grey) contours indicates the 1σ, 2σ and 3σ errors for the $\langle\kappa^2\rangle$ statistics and the cyan (light grey) contours are the same for the $\langle\kappa^3\rangle$. The covariance matrix contains both the cosmic variance and the statistical noise. Here the joint likelihood shown in filled contours is calculated by taking into the account the $\langle\kappa^2\rangle$-$\langle\kappa^3\rangle$ correlations at different scales.

17
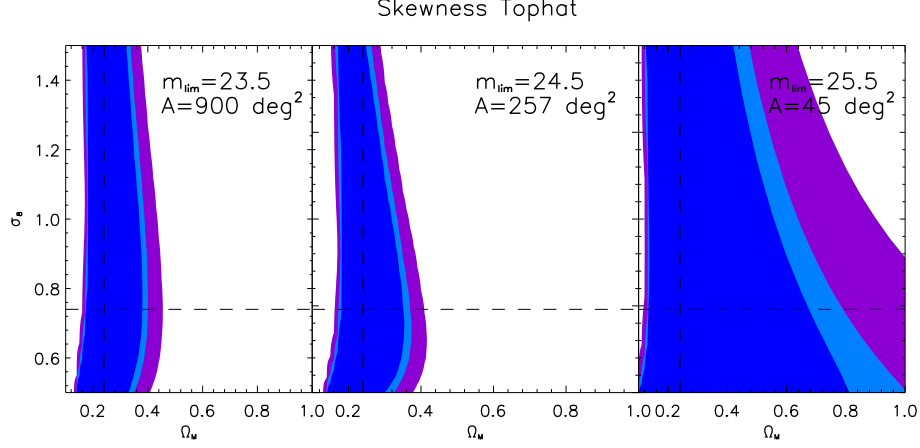
Figure 9: The likelihood analysis for various survey depths and areas with fixed observing time for skewness S_3 smoothed with the top-hat filter. The observing time is equal for all cases, while the survey area and depth vary. Table 2 shows the values for m_{lim} with the corresponding survey areas. The covariance matrix contains both the cosmic variance and the statistical noise. The skewness measurements are most optimal for shallower surveys.

the expected improvement for cosmological parameter constraints, using a combination of two- and three-point lensing statistics on the completed CFHTLS-wide survey was determined. A mock CFHTLS-wide survey type of 170 $\deg^2$ was generated using a limiting magnitude of $m_{lim} = 24.5$ (i-band) with $n_g=22$ galaxies per arcmin^2, $z_{med}=0.91$ and $\sigma_\epsilon=0.44$ and the potential contamination by residual systematics was ignored.

Figure 11 shows the Ω_m and σ_8 error contours from a joint measurement of $\langle\kappa^2\rangle$ and $\langle\kappa^3\rangle$ for the three filters used in this study. It is clear that the top-hat filter leads to a more significant degeneracy breaking between Ω_m and σ_8, which can be understood by the fact that this filter preserves modes with wavelengths larger than the smoothing size, while the aperture filters are not sensitive to large scale variations. The joint two- and three-point analysis of the completed CFHTLS-Wide will constrain Ω_m and σ_8 to 17% and 10% respectively. This corresponds to a gain factor (GF) of ~ 2.5 (for Ω_m) and ~ 2.1 (for σ_8) improvement on the two-point analysis alone when the top-hat filter is used. It is interesting to compare Figure 11 to a generalized χ^2 approach which can serve to quantify the performance of the different filters. The generalized χ^2 is defined as:

$$\frac{S}{N} = \sqrt{d^T * \mathbf{C}^{-1} * d} \tag{12}$$

where $\mathbf{C}$ is the covariance matrix of the statistics under consideration. The results for a 12.84 $\deg^2$ survey and limiting magnitude $m_{lim} = 24.5$ are shown
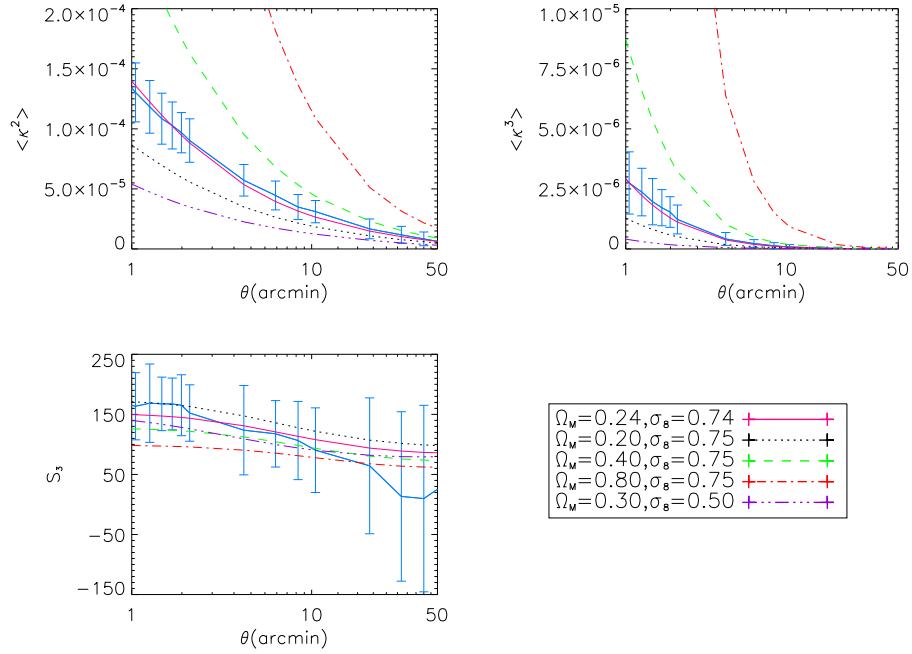
Figure 10: The comparison between the measured values of $\langle\kappa^2\rangle$, $\langle\kappa^3\rangle$ and S_3 and different cosmological models over a survey area of 12.84 deg^2. The blue line shows the measured data points, and the pink (solid) line is the fiducial model. The black (dotted), green (dashed) and red (dash-dotted) lines are models with the same $\sigma_8 = 0.75$ and values of $\Omega_m = 0.20, 0.40$ and 0.80 respectively, while the purple (dash-dot-dotted) line corresponds to a model with $\Omega_m = 0.30$ but $\sigma_8 = 0.50$. The plots show that the measurement of $\langle\kappa^2\rangle$ and $\langle\kappa^3\rangle$ are much more sensitive to the Ω_m, σ_8 parameters than the skewness S_3. This is why we can not currently constrain the Ω_m-σ_8 plane with skewness measurements.

in table 3, and they indicate that for two-point statistics the different filters are equivalent. The top-hat filter outperforms the aperture filters for the three-point statistics. It is a direct illustration that top-hat preserves small and large scale modes, and it is therefore more sensitive to non-linear effects. This invalidates the fact that the Compensated Gaussian filter is the most efficient measure of the skewness of the convergence [14]. The reason lies in the fact that for a fair comparison the maximum smoothing scale for Compensated Gaussian filter may not exceed a third of top-hat and aperture smoothing radii. This can be seen by looking at the equations which define the shape of the filters (see Section 3.4).

S/N	$\langle \kappa^2 \rangle$	$\langle \kappa^3 \rangle$	S_3
Top-hat	6.19	2.68	5.45
Aperture	6.05	1.61	2.17
Compensated Gaussian	6.93	1.88	3.24

Table 3: The generalized χ^2 results for top-hat, aperture and Compensated Gaussian filters. The full covariance matrix is that of the 12.84 deg^2 maps. The data d is from the κ-maps smoothed with top-hat, aperture and Compensated Gaussian filters. The correlation between the scales are contained in the signal-to-noise ratio.

The joint $\langle \kappa^2 \rangle$-$\langle \kappa^3 \rangle$ likelihood analysis with top-hat, aperture and Compensated Gaussian filters proved to be promising, whereas the skewness which is in principle a very interesting statistic inferred very weak cosmological constraints even for the current largest weak lensing survey at 170 deg^2. Figure 12 shows skewness likelihood contours obtained using both top-hat and Compensated Gaussian filter for CFHTLS-like survey confirming what stated above about the poor efficiency of the skewness.

One of the forthcoming weak lensing surveys is the KIlo Degree Survey (KIDS area of 1500 deg^2 at m_{lim}=23.5). We performed for the KIDS survey the same analysis as for the CFHTLS-Wide to forecast the accuracy of the likelihood constraints using two- and three-point shear statistics. Moreover, for comparison the calculations were repeated for a survey with the same observing time needed for the KIDS survey but different total area and depth. The results establish which survey design would be the most optimal to infer constraints using the joint two- and and three- point shear statistics. The expected likelihood contours for the complete KIDS survey are shown in the panel 13(a), whereas panel 13(b) shows the same results when a deeper (m_{lim}=24.5) and narrower (area=450 deg^2) survey given the same observing time was considered. As expected from Figure 8 the shallower KIDS gives better results for the joint likelihood, but the skewness would be slightly better measured from the deeper (m_{lim}=24.5) survey.

6. Conclusion and Discussion

We studied how useful the measurement of the two- and three-point shear statistics can be to derive cosmological constraints under realistic observing conditions. One of the limitations of the previous work on this topic was the
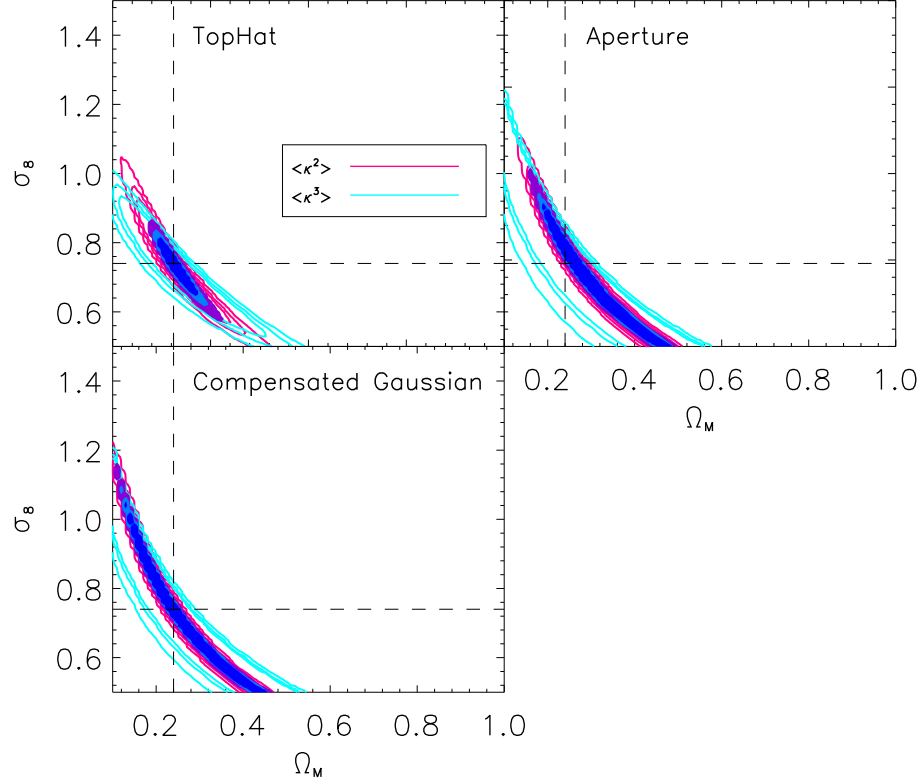
Figure 11: The cosmological constraints on Ω_m-σ_8 plane obtained with different smoothing filters. The contours show the $\langle\kappa^2\rangle$ and $\langle\kappa^3\rangle$ joint likelihood forecast based on CFHTLS completed area. The survey area is 170 deg^2 and the limiting magnitude is 24.5 with the full redshift distribution. Here the pink (dark grey) contours show the $\langle\kappa^2\rangle$ and the cyan (light grey) contours show the $\langle\kappa^3\rangle$ constraints. The filled contours correspond to the 1σ, 2σ and 3σ errors for the joint likelihood. The fiducial model used is a ΛCDM with $\Omega_m = 0.24$ and $\sigma_8 = 0.74$. The degeneracy direction of the $\langle\kappa^2\rangle$ and $\langle\kappa^3\rangle$ likelihood is different (especially when the maps are smoothed with Compensated Gaussian filter) so their joint likelihood results in a tighter constraints on the parameters. The joint likelihood here is calculated by taking into account the cross correlations between $\langle\kappa^2\rangle$ and $\langle\kappa^3\rangle$ at all scales.
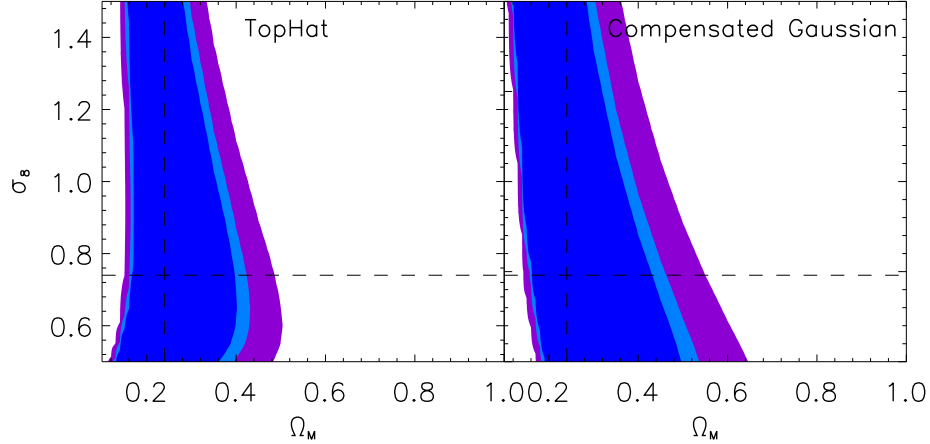
Figure 12: The skewness S_3 likelihood analysis for the CFHTLS-wide predictions. The smoothing filters top-hat and Compensated Gaussian are used. The aperture filter does not provide any constraint on the Ω_m-σ_8 plane for the given survey characteristics. The covariance matrix contains both the cosmic variance and the statistical noise.

disconnection between the source redshift distribution and the survey depth under consideration. Here, a set of ray-tracing simulations was populated with source galaxies that follow a redshift distribution and galaxy number density calibrated from real data.

We then investigated how well the parameters σ_8 and Ω_m can be measured with different smoothing filters for different survey depths. For a fixed observing time, the results of the study favored the medium depth and width survey over shallower and wider or deeper and narrower surveys. There is an optimal survey depth versus size for which the source density (survey depth) and cosmic variance (survey area) are balanced, which turns out to be very close to the CFHTLS depth. Our results can be applied also to surveys covering a large fraction of the sky with no limitation on the observing time (e.g. PanSTARRS and LSST) by a simply rescaling the covariance matrices. They can also be extended to space data if the amplitude of ellipticity noise and galaxy number counts are adjusted according to space observations (this is particularly relevant for a wide field space imager like the one by JDEM).

We find that the lensing statistics are best measured at scales between 1 to 30 arcminutes, where the contribution of statistical noise, cosmic variance and the mixed term are minimal. We also find that the different smoothing filters give similar results although the top-hat appears to include more modes and is therefore slightly better than the others. Combining $\langle \kappa^2 \rangle$ and $\langle \kappa^3 \rangle$ is promising to achieve cosmological constraints in the Ω_m-σ_8 parameter space. On the contrary the skewness of the convergence does not appear able of breaking the
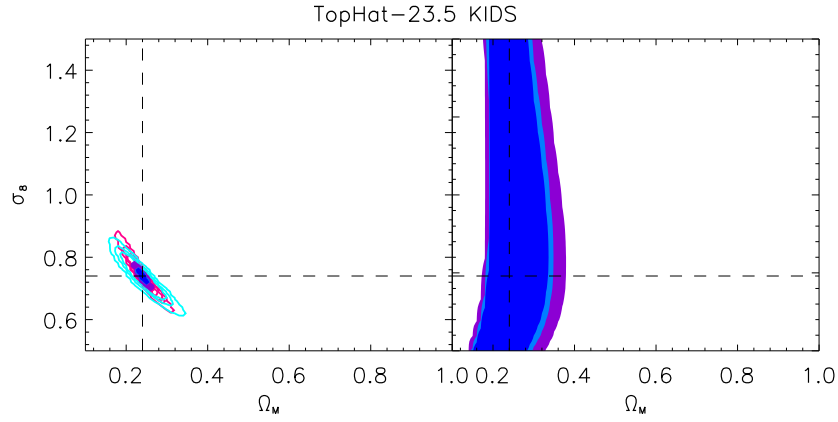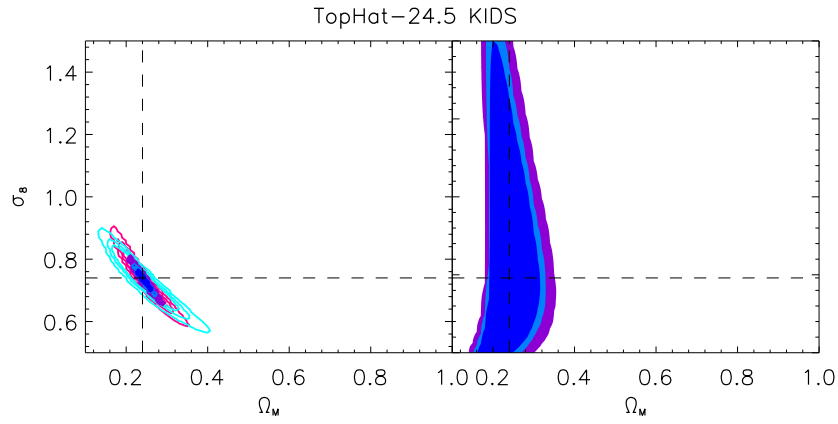
Figure 13: The comparison between a KIDS-like survey at two limiting magnitudes. The right panels show the likelihood contours of $\langle \kappa^2 \rangle$ and $\langle \kappa^3 \rangle$ smoothed with the top-hat filter. The left panels are the skewness contours. The survey area for the panel (a) is 1500 deg^2 as is planned for the KIDS survey with m_{lim}=23.5. In panel (b) the observing time is kept the same and the survey area if adjusted to 450 deg^2 for m_{lim}=24.5.

23

degeneracy between σ_8 and Ω_m as initially expected ([5] and [6]). The reason is that the cosmic variance on S_3 is comparable to the difference in lensing signal amplitude for the different cosmological models of interest. Only very large surveys will be able to measure the skewness accurately.

We forecasted the cosmological constraints for the CFHTLS-wide completed survey finding that the combination of two- and three-point functions on the CFHTLS will greatly enhance the measurement of σ_8 and Ω_m. A similar calculation showed the potential precision achievable with the future KIDS survey.

This study has some limitations which will be investigated in future work. One of them is the fact that the source galaxies are clustered in three dimensional space which overlap with lens redshift distribution (problem known as the source clustering problem, [25]). This effect leads to a change in the skewness of the convergence (by as much as 25%), and its impact on the three-point statistics has not been evaluated yet. A recent study also showed potential impact on the two-point statistics, although at a moderate level ([26]). Another limitation is the potential impact of intrinsic alignment on three-point statistics. This is particularly relevant for shallow surveys such as PanSTARRS or KIDS ([41]). This effect should be taken into the account as well. We would be able to investigate these two complications with ray-tracing simulations which include galaxies in dark matter halos; this can be realized by the use of semi analytical models such as the ones described in [26].

7. Acknowledgement

References

[1] J. Benjamin, C. Heymans, E. Semboloni, L. van Waerbeke, H. Hoekstra, T. Erben, M. D. Gladders, M. Hetterscheidt, Y. Mellier, and H. K. C. Yee. MNRAS, 381:702, 2007.

[2] L. Fu, E. Semboloni, H. Hoekstra, M. Kilbinger, L. van Waerbeke, I. Tereno, Y. Mellier, C. Heymans, J. Coupon, K. Benabed, J. Benjamin, E. Bertin, O. Doré, M. J. Hudson, O. Ilbert, R. Maoli, C. Marmo, H. J. McCracken, and B. Ménard. A&A, 479:9, 2008.

[3] E. Komatsu, J. Dunkley,M. R.Nolta, C. L.Bennett, B. Gold, G. Hinshaw, N. Jarosik, D. Larson, M. Limon, L. Page, D. N. Spergel, M. Halpern, R. S. Hill, A. Kogut, S. S. Meyer, G. S. Tucker, J. L. Weiland, E. Wollack, and E. L. Wright. ApJS, 180:330, 2009.

[4] I. Tereno, C. Schimd, J. P. Uzan, M. Kilbinger, F. H. Vincent and L. Fu. arXiv:0810.0555v2 [astro-ph], 2008.

[5] F. Bernardeau, L. van Waerbeke, and Y. Mellier. A&A, 322:1, 1997.

[6] L. van Waerbeke, F. Bernardeau, and Y. Mellier. A&A, 342:15, 1999.

[7] F. Bernardeau, L. van Waerbeke, and Y. Mellier. A&A, 397:405, 2003.

[8] U.-L. Pen, T. Zhang, L. van Waerbeke, Y. Mellier, P. Zhang, and J. Dubinski. ApJ, 592:664, 2003.

[9] M. Jarvis, M. Takada, B. Jain, and G. Bernstein. In *Bulletin of the American Astronomical Society*, 37, 2005.

[10] L. Van Waerbeke, Y. Mellier, M. Radovich, E. Bertin, M. Dantel-Fort, H. J. McCracken, O. Le Fèvre, S. Foucaud, J.-C. Cuillandre, T. Erben, B. Jain, P. Schneider, F. Bernardeau, and B. Fort. A&A, 374:757, 2001.

[11] M. Kilbinger and P. Schneider. A&A, 442:69, 2005.

[12] M. Takada and B. Jain. MNRAS 348:897, 2004.

[13] A. Amara and A. Réfrégier. MNRAS, 381:1018, 2007.

[14] T.-J. Zhang, U.-L. Pen, P. Zhang, and J. Dubinski. ApJ, 598:818, 2003.

[15] J. Miralda-Escude. ApJ, 380:1, 1991.

[16] N. Kaiser. ApJ, 388:272, 1992.

[17] D. N. Spergel, R. Bean, O. Doré, M. R. Nolta, C. L. Bennett, J. Dunkley, G. Hinshaw, N. Jarosik, E. Komatsu, L. Page, H. V. Peiris, L. Verde, M. Halpern, R. S. Hill, A. Kogut, M. Limon, S. S.Meyer, N. Odegard, G. S. Tucker, J. L. Weiland, E. Wollack, and E. L.Wright. ApJS, 170:377, 2007.

[18] H. Merz, U.-L. Pen, and H. Trac. *New Astronomy*, 10:393, 2005.

[19] J. A. Peacock and S. J. Dodds. MNRAS, 280:L19, 1986.

[20] R. Scoccimarro. MNRAS, 299:1097, 1998.

[21] O. Ilbert, S. Arnouts, H. J. McCracken, M. Bolzonella, E. Bertin, O. Le Fèvre, Y. Mellier, G. Zamorani, R. Pellò, A. Iovino, L. Tresse, V. Le Brun, D. Bottini, B. Garilli, D. Maccagni, J. P. Picat, R. Scaramella, M. Scodeggio, G. Vettolani, A. Zanichelli, C. Adami, S. Bardelli, A. Cappi,

S. Charlot, P. Ciliegi, T. Contini, O. Cucciati, S. Foucaud, P. Franzetti, I. Gavignaud, L. Guzzo, B. Marano, C. Marinoni, A. Mazure, B. Meneux, R. Merighi, S. Paltani, A. Pollo, L. Pozzetti, M. Radovich, E. Zucca, M. Bondi, A. Bongiorno, G. Busarello, S. de La Torre, L. Gregorini, F. Lamareille, G. Mathez, P. Merluzzi, V. Ripepi, D. Rizzo, and D. Vergani. A&A, 457:841, 2006.

[22] C. Heymans, M. White, A. Heavens, C. Vale, and L. van Waerbeke. MN-RAS, 371:750, 2006.

[23] L. van Waerbeke, M. White, H. Hoekstra, and C. Heymans. *Astroparticle Physics*, 26:91, 2006.

[24] L. van Waerbeke. MNRAS, 313:524, 2000.

[25] F. Bernardeau. A&A 338:375 1998.

[26] J. E. Forero-Romero, J. Blaizot, J. Devriendt, L. van Waerbeke and B. Guiderdoni. MNRAS, 379, 1507, 2007.

[27] P. Schneider, L. van Waerbeke, B. Jain, and G. Kruse. MNRAS, 296:873, 1998.

[28] L. van Waerbeke. A&A, 334:1, 1998.

[29] G. Efstathiou, M. Davis, S. D. M White, and C. S. Frenk. ApJS, 57:241, 1985.

[30] J. Salmon. ApJ, 460:59, 1996.

[31] P. Schneider, L. van Waerbeke, M. Kilbinger, and Y. Mellier. A&A, 396:1, 2002.

[32] B. Joachimi, P. Schneider, and T. Eifler. A&A, 477:43, 2008.

[33] E. Semboloni, L. van Waerbeke, C. Heymans, T. Hamana, S. Colombi, M. White and Y. Mellier. MNRAS, 375:L6, 2007.

[34] T. Eifler, M. Kilbinger and P. Schneider. A&A, 482:9, 2008.

[35] J. Pielorz, J. Rodiger, I. Tereno and P. Schneider. *arXiv:0907.1524v1 [astro-ph.CO]*, 2009.

[36] J. Hartlap, P. Simon, and P. Schneider. A&A, 464:399, 2007.

[37] G. Bernstein *arXiv:astro-ph/0109319v1*, 2001.

[38] H. Hoekstra, Y. Mellier, L. van Waerbeke, E. Semboloni, L. Fu, M. J. Hudson, L. C. Parker, I. Tereno, and K. Benabed. ApJ, 647:116, 2006.

[39] E. Semboloni, Y. Mellier, L. van Waerbeke, H. Hoekstra, I. Tereno, K. Benabed, S. D. J. Gwyn, L. Fu, M. J. Hudson, R. Maoli, and L. C. Parker. A&A, 452:51, 2006.

[40] L. C. Parker, H. Hoekstra,M. J. Hudson, L. van Waerbeke, and Y. Mellier. ApJ, 669:21, 2007.

[41] E. Semboloni, C. Heymans, L. van Waerbeke, and P. Schneider. MNRAS, 388, 991, 2008.